

RESEARCH ARTICLE | JULY 10 2024

Large-scale semi-organized rolls in a sheared convective turbulence: Mean-field simulations

A. Asulin; E. Tkachenko; N. Kleeorin ; A. Levy ; I. Rogachevskii  

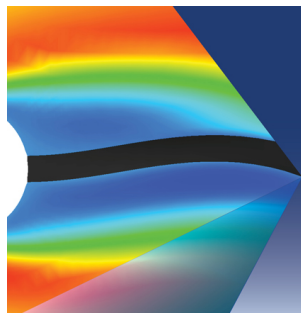


Physics of Fluids 36, 075131 (2024)

<https://doi.org/10.1063/5.0214459>



10 July 2024 14:13:34



Physics of Fluids

Special Topic:

Fluid-Structure Interaction

Guest Editors: A-Man Zhang, Tiegang Liu, Boo Cheong Khoo and Nhan Phan-Thien

[Submit Today!](#)

Large-scale semi-organized rolls in a sheared convective turbulence: Mean-field simulations

Cite as: Phys. Fluids **36**, 075131 (2024); doi: 10.1063/5.0214459

Submitted: 17 April 2024 · Accepted: 22 June 2024 ·

Published Online: 10 July 2024



View Online



Export Citation



CrossMark

A. Asulin,¹ E. Tkachenko,¹ N. Kleeorin,^{1,2}  A. Levy,¹  and I. Rogachevskii^{1,a)} 

AFFILIATIONS

¹The Pearlstone Center for Aeronautical Engineering Studies, Department of Mechanical Engineering, Ben-Gurion University of the Negev, P.O. Box 653, Beer-Sheva 84105, Israel

²Institute of Continuous Media Mechanics, Korolyov str. 1, 614013 Perm, Russia

^{a)} Author to whom correspondence should be addressed: gary@bgu.ac.il

ABSTRACT

Based on a mean-field theory of a non-rotating turbulent convection [T. Elperin *et al.*, Phys. Rev. E **66**, 066305, (2002)], we perform mean-field simulations (MFS) of sheared convection that takes into account an effect of modification of the turbulent heat flux by the non-uniform large-scale motions. This effect is caused by the production of additional essentially anisotropic velocity fluctuations generated by tangling of the mean-velocity gradients by small-scale turbulent motions due to the influence of the inertial forces during the lifetime of turbulent eddies. These anisotropic velocity fluctuations contribute to the turbulent heat flux. As the result of this effect, there is an excitation of large-scale convective-shear instability, which causes the formation of large-scale semi-organized structures in the form of rolls. The lifetimes and spatial scales of these structures are much larger compared to the turbulent scales. By means of MFS performed for stress-free and no-slip vertical boundary conditions, we determine the spatial and temporal characteristics of these structures. Our study demonstrates that the modification of the turbulent heat flux by non-uniform flows leads to a strong reduction of the critical effective Rayleigh number (based on the eddy viscosity and turbulent temperature diffusivity) required for the formation of the large-scale rolls. During the nonlinear stage of the convective-shear instability, there is a transition from a two-layer vertical structure with two rolls in the vertical direction before the system reaches steady-state to a one-layer vertical structure with one roll after the system reaches steady state. This effect is observed for all effective Rayleigh numbers. We find that inside the convective rolls, the spatial distribution of the mean potential temperature includes regions with a positive vertical gradient of the potential temperature caused by the mean heat flux of the convective rolls. This study might be useful for understanding the origin of large-scale rolls observed in atmospheric convective boundary layers, as well as in numerical simulations and laboratory experiments.

© 2024 Author(s). All article content, except where otherwise noted, is licensed under a Creative Commons Attribution (CC BY) license (<https://creativecommons.org/licenses/by/4.0/>). <https://doi.org/10.1063/5.0214459>

I. INTRODUCTION

Temperature stratified turbulence and turbulent convection exist in many geophysical and astrophysical flows as well as in industrial flows.^{1–7} Turbulence and associated turbulent transport were studied for more than 100 years. However, some key questions remain unclear due to extreme values of the governing parameters in geophysical and astrophysical flows.^{8–12}

Large-scale coherent structures in a developed convective turbulence have been seen in various laboratory experiments in the Rayleigh-Bénard setup,^{13–26} in the atmospheric convective turbulence,^{27–38} in direct numerical simulations,^{39–44} and in large-eddy simulations.^{45–49} Characteristic timescales and spatial scales of the coherent structures in a small-scale turbulent convection are much larger than the characteristic turbulent scales.

A mean-field theory of the coherent structures formed in convective turbulence has suggested that a redistribution of the turbulent heat flux by nonuniform large-scale motions is crucial in the formation of the large-scale coherent structures in a convective turbulence.^{50–52} This effect causes an excitation of a convective-wind instability in the shear-free turbulent convection resulting in the formation of large-scale motions in the form of cells. This phenomenon has been recently investigated by the mean-field numerical simulations,⁵³ which demonstrates that:

- The redistribution of the turbulent heat flux by the nonuniform large-scale motions results in a strong reduction of the critical effective Rayleigh number (based on the eddy viscosity and turbulent temperature diffusivity) required for the formation of the large-scale convective cells.

- The convective-wind instability is excited when the scale separation ratio between the height of the convective layer and the integral turbulence scale is large.
- The level of the mean kinetic energy at saturation increases with the increase of the scale separation ratio, and it is very weakly dependent on the effective Rayleigh number.
- Inside the large-scale convective cells, there are local regions with the positive vertical gradient of the potential temperature which implies that these regions are stably stratified.

In the sheared convective turbulence, the large-scale convective-shear instability results in an excitation of convective-shear waves, and the dominant coherent structures in the sheared convection are rolls.^{50–52} The goal of the present study is to perform mean-field numerical simulations in a sheared convection taking into account the effect of modification of the turbulent heat flux by non-uniform large-scale motions.

This paper is organized as follows. In Sec. II, we discuss physics related to a modification of the turbulent heat flux due to anisotropic velocity fluctuations in turbulence with non-uniform large-scale flows in a sheared convective turbulence. In Sec. III, we formulate the non-dimensional equations, the governing non-dimensional parameters and study the large-scale convective-shear instability. In Sec. IV, we describe the set-up for the mean-field simulations and discuss the numerical results. Finally, conclusions are drawn in Sec. V.

II. SHEARED TURBULENT CONVECTION AND TURBULENT HEAT FLUX

We consider sheared turbulent convection with very high Rayleigh numbers, and large Reynolds and Peclet numbers. To study formation and evolution of the semi-organized structures in a small-scale convective turbulence, we use a mean field approach. In the framework of this approach, the velocity \mathbf{U} , pressure P , and potential temperature Θ are decomposed into the mean fields and fluctuations, where $\mathbf{U} = \overline{\mathbf{U}} + \mathbf{u}$, $P = \overline{P} + p$ and $\Theta = \overline{\Theta} + \theta$. Since we use Reynolds averaging, fluctuations have zero mean values, where $\overline{\mathbf{U}} = \langle \mathbf{U} \rangle$ is the mean velocity, $\overline{P} = \langle P \rangle$ is the mean pressure and $\overline{\Theta} = \langle \Theta \rangle$ is the mean potential temperature, and \mathbf{u} , p , and θ are fluctuations of velocity, pressure, and potential temperature, respectively. Averaging the Navier–Stokes equation and equation for the potential temperature over an ensemble, we arrive at the mean-field equations written in the Boussinesq approximation with $\text{div } \overline{\mathbf{U}} = 0$,

$$\left[\frac{\partial}{\partial t} + (\overline{\mathbf{U}} + \overline{\mathbf{U}}_S) \cdot \nabla \right] \overline{\mathbf{U}} + (\overline{\mathbf{U}} \cdot \nabla) \overline{\mathbf{U}}_S = -\frac{\nabla \overline{P}}{\overline{\rho}_0} - \nabla \cdot \hat{\mathbf{R}} + \beta \overline{\Theta} \mathbf{e}_z, \quad (1)$$

$$\left[\frac{\partial}{\partial t} + (\overline{\mathbf{U}} + \overline{\mathbf{U}}_S) \cdot \nabla \right] \overline{\Theta} = -(\overline{\mathbf{U}} \cdot \nabla) \overline{T}_0 - \nabla \cdot \langle \mathbf{u}\theta \rangle, \quad (2)$$

where $\hat{\mathbf{R}} \equiv R_{ij} = \langle u_i u_j \rangle$ is the Reynolds stress, $\overline{\mathbf{U}}_S = (Sz, 0, 0)$ is the shear velocity directed along the x axis, $\overline{\Theta}$ is the mean potential temperature defined as $\overline{\Theta} = \overline{T} (\overline{P}_0/\overline{P})^{1-1/\gamma}$. Here $\beta = |g|/T_0$ is the buoyancy parameter, $\mathbf{g} = -g \mathbf{e}_z$ is the acceleration caused by the gravity, \mathbf{e}_z is the unit vector in the vertical direction (along the z axis), $\gamma = c_p/c_v$ is the specific heats ratio, \overline{T} is the mean physical temperature with the reference value \overline{T}_0 as the temperature in the equilibrium (i.e., the basic reference state), \overline{P} is the mean pressure with the reference value \overline{P}_0

and $\overline{\rho}_0$ is the mean fluid density in the equilibrium. For large Reynolds and Peclet numbers, we neglect in Eqs. (1) and (2) small terms due to the kinematic viscosity and molecular diffusivity of the potential temperature in comparison with those due to the turbulent viscosity and turbulent diffusivity. In Eqs. (1) and (2), the mean fields correspond to deviations from the equilibrium: $\overline{\mathbf{U}}_0 = \overline{\mathbf{U}}_S$, $\nabla \overline{P}_0 = \overline{\rho}_0 \mathbf{g}$, and $\overline{\rho}_0 = \text{const}$.

The effects of small-scale convective turbulence on the mean fields are described by the Reynolds stress $\langle u_i u_j \rangle$ and turbulent flux of potential temperature $\mathbf{F} = \langle \mathbf{u}\theta \rangle$. In the classical concept of down-gradient turbulent transport, the basic second-order moments (e.g., the Reynolds stress and the turbulent flux of potential temperature) are assumed to be proportional to the local mean gradients, whereas the proportionality coefficients, namely turbulent viscosity ν_T and turbulent temperature diffusivity κ_T , are determined by local turbulent parameters. For instance, the Reynolds stress is $\langle u_i u_j \rangle = -2\nu_T (\nabla_i \overline{U}_j + \nabla_j \overline{U}_i)$, while the turbulent heat flux is given by $\mathbf{F} = -\kappa_T \nabla \overline{\Theta}$.⁸

In turbulent convection with semi-organized structures (e.g., large-scale circulations and large-scale convective rolls), the mean velocity and temperature fields inside the semi-organized structures are strongly nonuniform. These nonuniform large-scale motions produce strongly anisotropic velocity fluctuations which contribute to the turbulent heat flux. As has been shown in Refs. 50 and 51, the turbulent heat flux \mathbf{F} , which takes into account anisotropic velocity fluctuations, reads

$$\mathbf{F} = \mathbf{F}^* - \tau_0 \left[\mathbf{F}_z^* \text{div } \overline{\mathbf{U}}_{\perp} - \frac{1}{2} (\overline{\mathbf{W}} \times \mathbf{F}_z^*) - \frac{1}{2} (\overline{\mathbf{W}}_z \times \mathbf{F}_x^{\text{CW}}) \right], \quad (3)$$

where $\mathbf{F}_x^{\text{CW}} = -\tau_0 (\mathbf{F}_z^* \cdot \nabla) \overline{\mathbf{U}}_S(z)$ is the counter-wind turbulent heat flux and $\mathbf{F}^* = -\kappa_T \nabla \overline{\Theta}$ is the classical turbulent heat flux, τ_0 is the correlation time of turbulent velocity at the integral scale of turbulent motions, $\overline{\mathbf{W}} = \nabla \times \overline{\mathbf{U}}$ is the mean vorticity, $\overline{\mathbf{U}} = \overline{\mathbf{U}}_{\perp} + \overline{\mathbf{U}}_z$ is the mean velocity with the horizontal $\overline{\mathbf{U}}_{\perp}$ and vertical $\overline{\mathbf{U}}_z$ components. Equation (3) is derived for large Reynolds and Peclet numbers, which implies that turbulent viscosity and turbulent diffusivity are much larger than the molecular viscosity and molecular diffusivity, respectively. The additional terms in the turbulent heat flux result in the excitation of large-scale instability and formation of the large-scale convective rolls.^{50–52}

The physics related to the additional terms in the turbulent heat flux is discussed below. The term $-\tau_0 \mathbf{F}_z^* \text{div } \overline{\mathbf{U}}_{\perp}$ in Eq. (3) for the turbulent heat flux causes the redistribution of the vertical background turbulent heat flux \mathbf{F}_z^* by the perturbations of the convergent (or divergent) horizontal mean velocity $\overline{\mathbf{U}}_{\perp}$ (see Fig. 1) during the lifetime of turbulent eddies. This enhances the vertical turbulent flux of potential temperature due to the converging horizontal motions, which increases the buoyancy, thus creating the upward flow. The latter increases the horizontal convergent flow.

On the other hand, the term $(\tau_0/2) (\overline{\mathbf{W}} \times \mathbf{F}_z^*)$ in Eq. (3) produces the horizontal turbulent heat flux by the “rotation” of the vertical background turbulent heat flux \mathbf{F}_z^* caused by the perturbations of the horizontal mean vorticity $\overline{\mathbf{W}}_{\perp}$. This decreases local potential temperatures in rising motions, which decreases the buoyancy accelerations, and weakens vertical velocity and vorticity.

The last term $(\tau_0/2) (\overline{\mathbf{W}}_z \times \mathbf{F}_x^{\text{CW}})$ in Eq. (3) for the turbulent heat flux produces the horizontal heat flux through the “rotation” of the horizontal background counter-wind turbulent heat flux \mathbf{F}_x^{CW} by

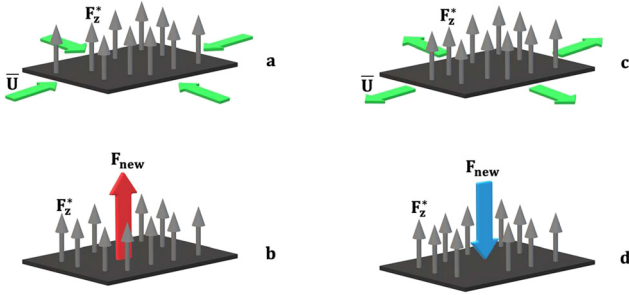


FIG. 1. The illustration of the physics caused by the new turbulent heat flux $F_{\text{new}} = -\tau_0 F_z^* \text{div} \bar{U}_\perp$ produced by the perturbations of the convergent (or divergent) horizontal mean flows \bar{U}_\perp (shown by the green arrows in panels a and c). The new turbulent flux F_{new} increases the upward turbulent heat flux, enhances buoyancy and increases the local mean potential temperature, thus creating the upward flow. Likewise, the new turbulent flux F_{new} decreases the vertical turbulent flux of potential temperature by the divergent horizontal motions, which reduces the buoyancy and decreases the local mean potential temperature, thus creating the downward flow. These effects create the large-scale circulation.

the vertical component of the mean vorticity. The counter-wind turbulent flux of potential temperature F_x^{CW} arises due to the following reasons. In a horizontally homogeneous and sheared convective turbulence, the mean shear velocity $\bar{U}_x^s(z)$ increases with the height, while the mean potential temperature $\bar{\Theta}(z)$ decreases with the height. Uprising fluid particles produce both, positive fluctuations of potential temperature, $\theta > 0$ because $\partial\theta/\partial t \sim -(\mathbf{u} \cdot \nabla)\bar{\Theta}(z)$, and negative fluctuations of horizontal velocity, $u_x < 0$ because $\partial u_x/\partial t \sim -(\mathbf{u} \cdot \nabla)\bar{U}_x^s(z)$. This creates a negative horizontal turbulent flux of potential temperature, $u_x \theta < 0$. On the other hand, sinking fluid particles create both, negative fluctuations of potential temperature, $\theta < 0$, and positive fluctuations of horizontal velocity, $u_x > 0$, resulting in negative horizontal turbulent flux of potential temperature, $u_x \theta < 0$. Therefore, the net horizontal turbulent flux of potential temperature is negative, $F_x^{\text{CW}} \equiv \langle u_x \theta \rangle < 0$, in spite of a zero horizontal mean temperature gradient. Therefore, the counter-wind turbulent flux of potential temperature modifies the turbulent potential temperature flux caused by the non-uniform mean velocity field. The counter-wind turbulent flux is associated with non-gradient turbulence transport of heat.

The last term $(\tau_0/2) \bar{W}_z \times \mathbf{F}_x^{\text{CW}}$ in Eq. (3), causes generation of the cross-wind horizontal turbulent heat flux by turning the counter-wind horizontal turbulent flux F_x^{CW} by perturbations of vertical component of the mean vorticity \bar{W}_z (see Fig. 2). This produces alternating pairs of convergence or divergence cross-wind turbulent heat fluxes, $F_y^{\text{new}} = (\tau_0/2) \bar{W}_z \times \mathbf{F}_x^{\text{CW}}$, resulting alternative warmer or cooler patches which, in turn, cause alternative upward warm and downward cool motions. This is precisely the mechanism of large-scale instability responsible for the formation of the large-scale convective rolls stretched along the mean velocity shear (see Fig. 3) and generation of convective-shear waves propagating perpendicular to the convective rolls in the sheared convection.^{50–52}

III. GOVERNING EQUATIONS AND CONVECTIVE-SHEAR INSTABILITY

Using the expression (3) for the turbulent heat flux \mathbf{F} with the additional terms caused by the non-uniform mean flows, calculating

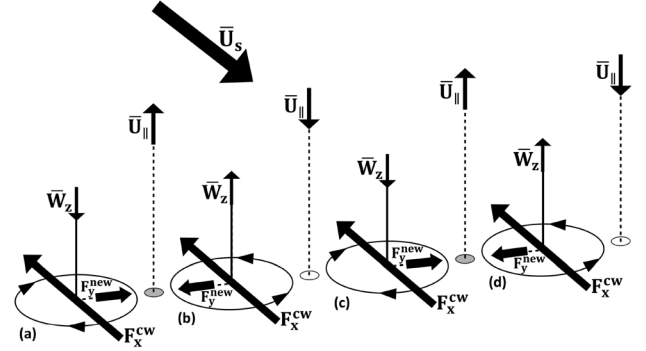


FIG. 2. The mechanism of formation of large-scale convective rolls stretched along the shear velocity $\bar{U}_s(z)$. Horizontal counter-wind turbulent heat flux F_x^{CW} is turned by perturbations of vertical vorticity \bar{W}_z , i.e., this effect creates alternating pairs of convergence or divergence cross-wind turbulent heat fluxes, $F_y^{\text{new}} = (\tau_0/2) \bar{W}_z \times \mathbf{F}_x^{\text{CW}}$, which are clockwise or opposite rotations of air columns. This effect causes converging turbulent heat fluxes with warm patch between the pair (a) and (b) of columns in the FIG, and diverging turbulent heat fluxes with cool patch between the pair (b) and (c) in the FIG. The warm patch causes an updraft and cool patch produces a downdraft, whereas the mean shear velocity $\bar{U}_s(z)$ stretches the flow pattern and completes creation of the large-scale convective rolls.

div \mathbf{F} , and assuming that the non-dimensional total vertical heat flux $\Phi_c = \tilde{F}_z^* + \tilde{U}_z \bar{\Theta}$ is constant, we rewrite Eqs. (1) and (2) in a non-dimensional form as

$$\frac{\partial \tilde{\mathbf{U}}}{\partial t} + [(\tilde{\mathbf{U}} + \tilde{\mathbf{U}}_s) \cdot \nabla] \tilde{\mathbf{U}} + (\tilde{\mathbf{U}} \cdot \nabla) \tilde{\mathbf{U}}_s = -\frac{\nabla \tilde{P}}{\rho_0} + \text{Ra}_T \tilde{\Theta} \mathbf{e}_z + \Delta \tilde{\mathbf{U}}, \quad (4)$$

$$\begin{aligned} \text{Pr}_T \left(\frac{\partial \tilde{\Theta}}{\partial t} + [(\tilde{\mathbf{U}} + \tilde{\mathbf{U}}_s) \cdot \nabla] \tilde{\Theta} \right) &= \tilde{U}_z + \Delta \tilde{\Theta} + \frac{\epsilon}{2} \left\{ (\Phi_c - \tilde{U}_z \tilde{\Theta}) \right. \\ &\times \left[(\Delta - 2\nabla_z^2) \tilde{U}_z + \text{Sh} (\nabla_y^2 \tilde{U}_x - \nabla_x \nabla_y \tilde{U}_y) \right] \\ &+ 2(\nabla_z \tilde{U}_z) \nabla_z (\tilde{U}_z \tilde{\Theta}) + (\nabla_z \tilde{U}_x - \nabla_x \tilde{U}_z) \nabla_x (\tilde{U}_z \tilde{\Theta}) \\ &\left. + [\nabla_z \tilde{U}_y - \nabla_y \tilde{U}_z + \text{Sh} (\nabla_x \tilde{U}_y - \nabla_y \tilde{U}_x)] \nabla_y (\tilde{U}_z \tilde{\Theta}) \right\}, \end{aligned} \quad (5)$$

where the non-dimensional mean velocity $\tilde{\mathbf{U}}$ with $\text{div} \tilde{\mathbf{U}} = 0$, the mean potential temperature $\tilde{\Theta}$ and the mean pressure \tilde{P} are shown with tilde, the flux F_z^* is the nondimensional vertical turbulent background heat flux, the unit vector \mathbf{e}_z is directed along vertical z axis, the non-dimensional shear velocity is $\tilde{U}_s = (\text{Sh} \tilde{z}, 0, 0)$, and \tilde{z} is the non-dimensional vertical coordinate.

Equations (4) and (5) are written in non-dimensional form, where length is measured in the units of the vertical size of the convective layer L_z , time is measured in the units of the turbulent viscosity time, L_z^2/ν_T , velocity is measured in the units of ν_T/L_z , potential temperature is measured in the units of $L_z N^2 \text{Pr}_T/\beta$ and pressure is measured in the units of $\rho_0 (\nu_T/L_z)^2$. Here $\nu_T = u_0 \ell_0/3$ is the turbulent (eddy) viscosity, u_0 is the r.m.s. turbulent velocity, ℓ_0 is the turbulent integral scale and $N^2 = \beta |\nabla_z \bar{T}_{\text{eq}}|$.

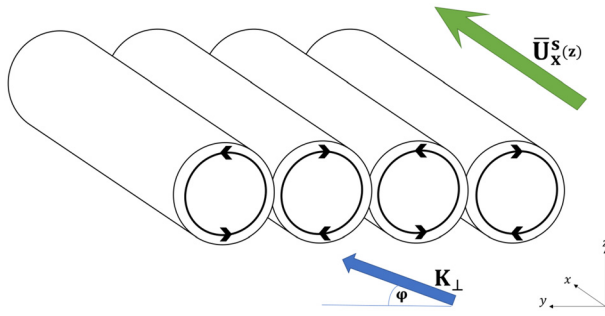


FIG. 3. Large-scale convective rolls stretched along the mean velocity shear and generation of convective-shear waves propagating perpendicular to the convective rolls.

We use the following dimensionless parameters appeared in Eqs. (4) and (5):

- the effective Rayleigh number:

$$Ra_T = \frac{L_z^4 N^2}{\nu_T \kappa_T}, \quad (6)$$

- the turbulent Prandtl number:

$$Pr_T = \frac{\nu_T}{\kappa_T}, \quad (7)$$

- the scale separation parameter:

$$\epsilon = \frac{\ell_0^2}{3L_z^2}, \quad (8)$$

- the non-dimensional total vertical heat flux:

$$\Phi_c = \frac{3}{\epsilon^2 Ra_T} \left(\frac{u_c}{u_0} \right)^3, \quad (9)$$

- the non-dimensional shear number:

$$Sh = \frac{S \tau_0}{\epsilon}, \quad (10)$$

where $S = \nabla_z \bar{U}_x^s$ is the linear velocity shear, i.e., S is constant, $u_c = (gF_z \ell_0)^{1/3}$ is the convective velocity, F_z is the vertical turbulent flux of potential temperature, κ_T is the turbulent (eddy) diffusivity and $\tau_0 = \ell_0/u_0$. In Eqs. (4) and (5), we have neglected small terms $\sim O(\epsilon^2)$.

For analytical study of the large-scale instability, we consider for simplicity the two-dimensional problem when the mean fields are independent of the coordinate x . The non-dimensional shear velocity, $\tilde{U}_S = (Sh \tilde{z}, 0, 0)$, is directed along the x axis, so that the vorticity $\tilde{W}_S \equiv \nabla \times \tilde{U}_S$ is $\tilde{W}_S = (0, Sh, 0)$. We will start our analysis with the linear problem for small perturbations applying the linearized equations (4) and (5), to find the growth rate of the large-scale convective-shear instability. To this end, we calculate $[\nabla \times (\nabla \times \tilde{U})]_z$ using the linearized equation (4) to exclude the pressure term and we seek for solution of the obtained equations in the following form: $\tilde{U}(t, \mathbf{x}) = \tilde{U}_0 \exp[\gamma t - i(K_y y + K_z z)]$ and $\tilde{\Theta}(t, \mathbf{x}) = \tilde{\Theta}_0 \exp[\gamma t - i(K_y y + K_z z)]$. This yields the following system of algebraic equations:

$$(\gamma + K^2) \tilde{U}_z + Ra_T \left(\frac{K_z^2}{K^2} - 1 \right) \tilde{\Theta} = 0, \quad (11)$$

$$\left[1 + \frac{\sigma}{2\epsilon Ra_T} \left(2K_z^2 - K^2 + \frac{Sh^2 K_y^2}{\gamma + K^2} \right) \right] \tilde{U}_z - (\gamma + K^2) \tilde{\Theta} = 0, \quad (12)$$

where $\sigma = 3(u_c/u_0)^3$, $K = (K_y^2 + K_z^2)^{1/2}$, and we consider, for simplicity, the case when the turbulent Prandtl number $Pr_T = 1$. Equations (11) and (12) yield the equation for $\bar{\gamma} = (\gamma + K^2)/\gamma_0$ as

$$\bar{\gamma}^3 - \bar{\gamma} - \frac{\pi^2 \sigma Sh^2 \alpha^4}{2\epsilon \gamma_0^3 (1 + \alpha^2)} = 0, \quad (13)$$

where

$$\gamma_0 = \frac{\alpha}{(1 + \alpha^2)^{1/2}} \left[Ra_T + \frac{\pi^2 \sigma}{2\epsilon} (1 - \alpha^2) \right]^{1/2}, \quad (14)$$

$\alpha = K_y/K_z$ and $K_z = \pi$. This implies that $K_y = \alpha\pi$ and $K = (K_y^2 + K_z^2)^{1/2} = \pi(1 + \alpha^2)^{1/2}$. When

$$Ra_T < \frac{\pi^2 \sigma}{2\epsilon} (\alpha^2 - 1), \quad (15)$$

γ_0 is a complex function.

Generally, the solution of the cubic equation (13) describes two complex conjugate roots and one real negative root, which determine a damping mode. In the case of the complex conjugate roots, the instability can result in an excitation of convective-shear waves with the frequency $\omega = \text{Im}\{\gamma_0 \bar{\gamma}\}$ and the growth rate of the instability $\gamma_{\text{inst}} = \text{Re}\{\gamma_0 \bar{\gamma}\} - \pi^2(1 + \alpha^2)$, where $\text{Re}\{Z\}$ is the real part of the complex number and $\text{Im}\{Z\}$ is the imagine part of the complex number.

Numerical solution of Eq. (13) yields the growth rate γ_{inst} of the instability and the frequency ω of the excited convective-shear waves vs the parameter α for the effective Rayleigh numbers $Ra_T = 0.5$ (see Fig. 4) and $Ra_T = 10^3$ (see Fig. 5), and for different values of the non-dimensional shear number Sh . Figures 4 and 5 show that the convective-shear waves are excited for $\alpha > 1$ at small effective Rayleigh numbers and for $\alpha > 1.3$ at large effective Rayleigh numbers. The growth rate of the instability and the frequency of the excited convective-shear waves are very weakly dependent on the effective Rayleigh numbers. Increase of shear, results in increase in the growth rate γ_{inst} of the instability and the frequency of the excited convective-shear waves ω . The asymptotic solution of Eq. (13) in the case of $\gamma_{\text{inst}} \gg \gamma_0$ reads

$$\gamma_{\text{inst}} = \left(\frac{\pi^2 \sigma Sh^2 \alpha^4}{2\epsilon^3 (1 + \alpha^2)} \right)^{1/3} - \pi^2 (1 + \alpha^2), \quad (16)$$

which corresponds to a non-oscillatory growing solution with $\omega = 0$.

This instability causes formation of large-scale fluid motions in the form of rolls stretched along the imposed mean wind. This mechanism can also cause the generation of the convective-shear waves with the frequency shown in bottom panels of Figs. 4 and 5. The convective-shear waves propagate perpendicular to convective rolls. The predicted motions in convective rolls are characterized by nonzero helicity, in agreement with numerical simulations.²⁸ Note that similar

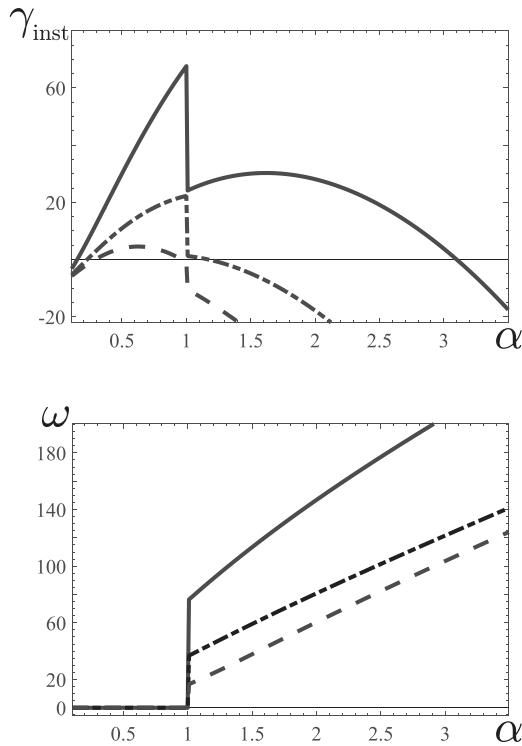


FIG. 4. The growth rate γ_{inst} of the instability (upper panel) and the frequency of the excited convective-shear waves ω (bottom panel) vs the parameter α for the effective Rayleigh number $\text{Ra}_T = 0.5$ and different values of the non-dimensional shear number $\text{Sh} = 0.03$ (dashed); 0.1 (dashed-dotted); 0.3 (solid).

waves propagating in the direction normal to cloud streets (convective rolls) have been detected in atmospheric convective boundary layers.³¹ This large-scale instability is fed by the energy of the convective turbulence.

IV. RESULTS OF MEAN-FIELD NUMERICAL SIMULATIONS

In this section, we discuss results of mean-field numerical simulations for three-dimensional problem. We solve numerically Eqs. (4) and (5) for the periodic boundary conditions in the horizontal xy plane. The boundary conditions for the potential temperature in the vertical direction are $\tilde{\Theta}(t, z = 0) = \tilde{\Theta}(t, z = 1) = 0$. We adopt the stress-free and no-slip boundary conditions for the velocity field in the vertical direction (along the z axis). The stress-free boundary conditions imply

$$\tilde{U}_z(t, z = 0) = \tilde{U}_z(t, z = 1) = 0, \quad (17)$$

$$\nabla_z \tilde{U}_x(t, z = 0) = \nabla_z \tilde{U}_x(t, z = 1) = 0, \quad (18)$$

$$\nabla_z \tilde{U}_y(t, z = 0) = \nabla_z \tilde{U}_y(t, z = 1) = 0, \quad (19)$$

while the no-slip boundary conditions are given by

$$\tilde{U}(t, z = 0) = \tilde{U}(t, z = 1) = 0. \quad (20)$$

To solve Eqs. (4) and (5), we use the ANSYS FLUENT code (version 19.2) in the 3D box $L_x = 5L_z$ and $L_y = L_z$, which is based on the

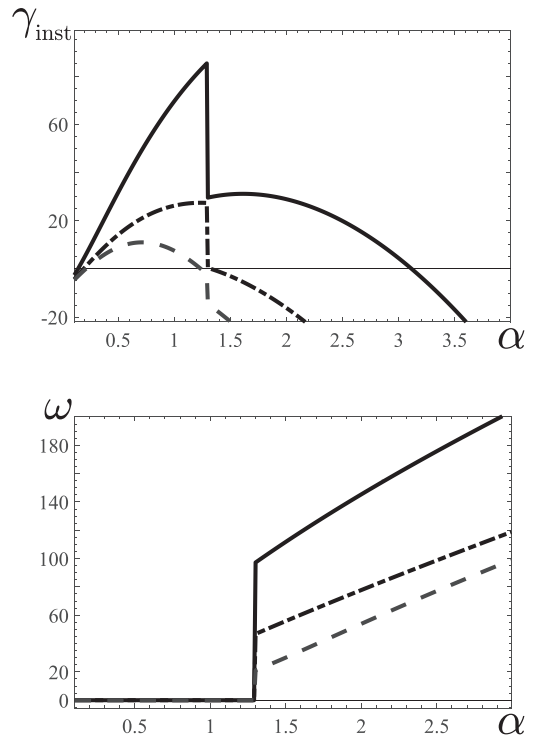


FIG. 5. The growth rate γ_{inst} of the instability (upper panel) and the frequency of the excited convective-shear waves ω (bottom panel) vs the parameter α for the effective Rayleigh number $\text{Ra}_T = 10^3$ and different values of the non-dimensional shear number $\text{Sh} = 0.03$ (dashed); 0.1 (dashed-dotted); 0.3 (solid).

finite volume method. The discretization method in the code is the second order. The simulations are performed with the spatial resolution $500 \times 100 \times 100$ in x , y , and z directions, respectively. A sensitivity check has been also made for the spatial resolution $500 \times 200 \times 200$. For both cases, similar results for velocity and potential temperature have been obtained. In all simulations, we use a time step of 10^{-3} . A sensitivity check has been made for time steps as well. Time steps of 10^{-3} and 2×10^{-3} have been tested and a maximum error of 0.05% at velocity and potential temperature between the time steps has been obtained. In addition, a convergence error was set to be less than 10^{-6} .

In the mean-field numerical simulations, we use the following values of the basic dimensionless parameters: the turbulent Prandtl number $\text{Pr}_T = 1$, the ratio $u_c/u_0 = 1$, the effective Rayleigh number changes from $\text{Ra}_T = 0.5$ to $\text{Ra}_T = 1800$ and the scale separation parameter ϵ varies from $\epsilon = 10^{-3}$ to 10^{-2} . The non-dimensional shear number Sh varies from $\text{Sh} = 0.01$ to $\text{Sh} = 1$. Note that the measurements of the two-point correlation function of the turbulent velocity field in the laboratory experiments with turbulent convection^{25,26,54} and DNS^{55,56} show that the integral turbulent scale ℓ_0 varies from $L_z/10$ to $L_z/5$, which corresponds to ϵ used in our mean-field simulations.

For illustration, in Figs. 6 and 7 we plot the time evolution of the maximum value $\tilde{U}_{\text{max}}(t)$ of the velocity magnitude $|\tilde{U}|$ for different values of the effective Rayleigh numbers Ra_T changing from 0.5 to 10^3 at a fixed value of the scale separation parameter ϵ between the vertical size L_z of the computational domain and the integral

turbulence scale ℓ_0 in the sheared large-scale convection (for $Sh = 1$), while in Figs. 8–11 we show the time evolution of the maximum velocity $\tilde{U}_{max}(t)$ for different values of the scale separation parameter ϵ (from 10^{-3} to 10^{-2}) (see Figs. 8 and 9 for $Ra_T = 0.5$ and Figs. 10 and 11 for $Ra_T = 10^3$). As can be seen in Figs. 6–11, at the initial stage of the evolution, the maximum velocity $\tilde{U}_{max}(t)$ increases in time exponentially due to the excitation of the large-scale convective-shear instability. The growth rate of the instability predicted from the theory [as the solution of the cubic dispersion equation (13)] is in agreement with that obtained in the mean-field numerical simulations.

During the nonlinear stage of the instability, we observe that $\tilde{U}_{max}(t)$ reaches the maximum value which is weakly dependent on the effective Rayleigh number Ra_T for the stress-free and no-slip boundary conditions (see Figs. 6 and 7). On the other hand, the maximum value of the function \tilde{U}_{max} at the stationary stage strongly depends on the scale separation parameter ϵ and on the boundary conditions (see Figs. 8 and 9). In particular, increasing the scale separation between the vertical size L_z of the computational domain and the integral turbulence scale ℓ_0 (i.e., decreasing the parameter ϵ), the maximum value of the function \tilde{U}_{max} increases. For the no-slip vertical boundary conditions, the large-scale instability is excited and convective structures are formed when $\epsilon < 3 \times 10^{-3}$ at $Ra_T = 0.5$, $\epsilon < 4 \times 10^{-3}$ at $Ra_T = 500$, and $\epsilon < 7 \times 10^{-3}$ at $Ra_T = 10^3$. In addition, the time evolution in the nonlinear stage of the instability for the stress-free and no-slip boundary conditions are different.

Some features in the time evolution of the maximum velocity $\tilde{U}_{max}(t)$ have been also observed in the recent mean-field simulations of the shear-free convection,⁵³ where $\tilde{U}_{max}(t)$ is independent of Ra_T for the same boundary conditions, but it strongly depends on the scale separation parameter ϵ . However, in a sheared large-scale convection, we do not observe clear nonlinear oscillations of \tilde{U}_{max} which have

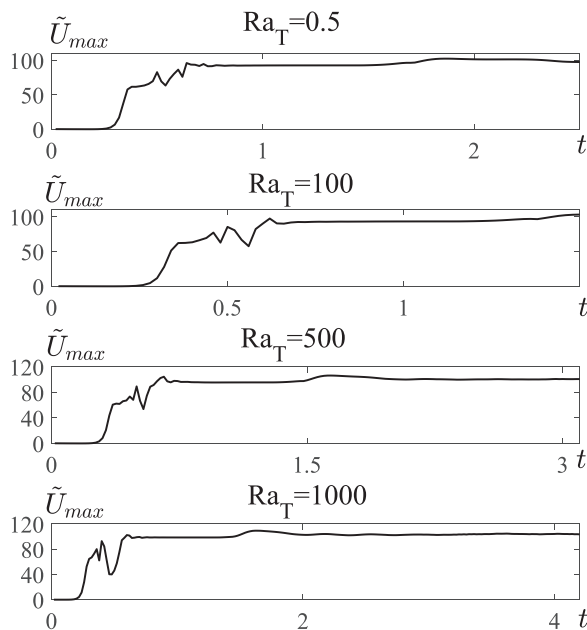


FIG. 6. Time evolution of the maximum velocity $\tilde{U}_{max}(t)$ for $\epsilon = 10^{-3}$, $\alpha = 0.5$ and shear number $Sh = 1$, and at different values of the effective Rayleigh number $Ra_T = 0.5, 100, 500$, and 1000 for the stress-free boundary conditions.

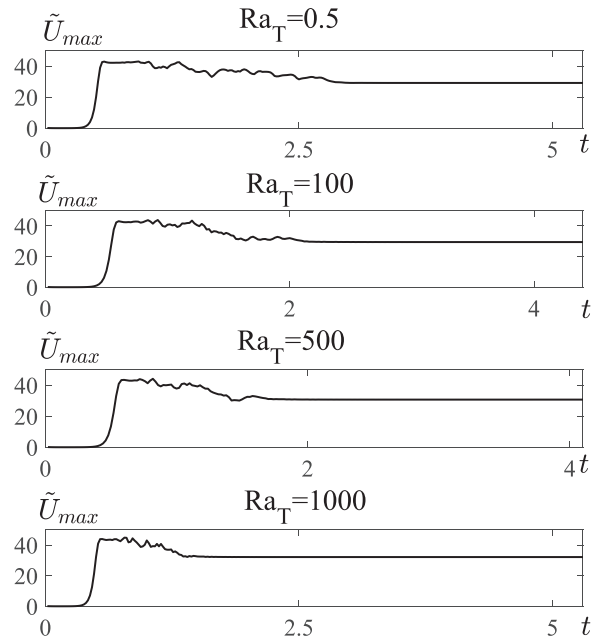


FIG. 7. Time evolution of the maximum velocity $\tilde{U}_{max}(t)$ for $\epsilon = 10^{-3}$, $\alpha = 0.5$ and shear number $Sh = 1$, and at different values of the effective Rayleigh number $Ra_T = 0.5, 100, 500$, and 1000 for the no-slip boundary conditions.

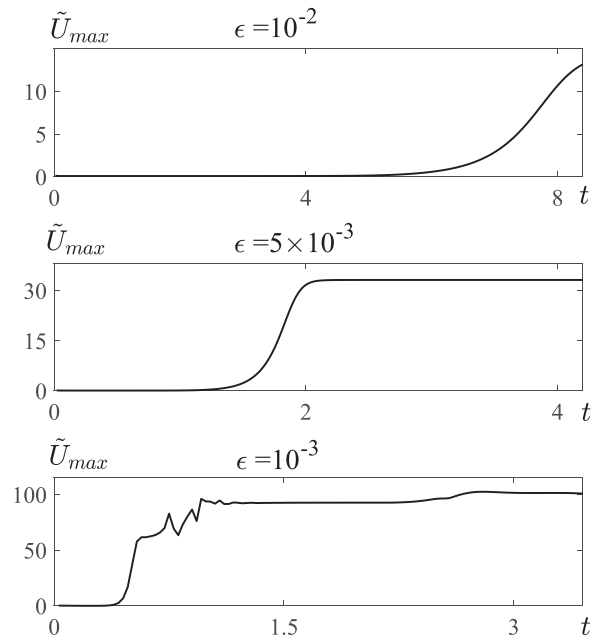


FIG. 8. Time evolution of the maximum velocity $\tilde{U}_{max}(t)$ for the effective Rayleigh number $Ra_T = 0.5$, $\alpha = 0.5$ and shear number $Sh = 1$, and at different values of the scale separation parameter $\epsilon = 10^{-3}, 5 \times 10^{-3}, 10^{-2}$, for the stress-free boundary conditions.

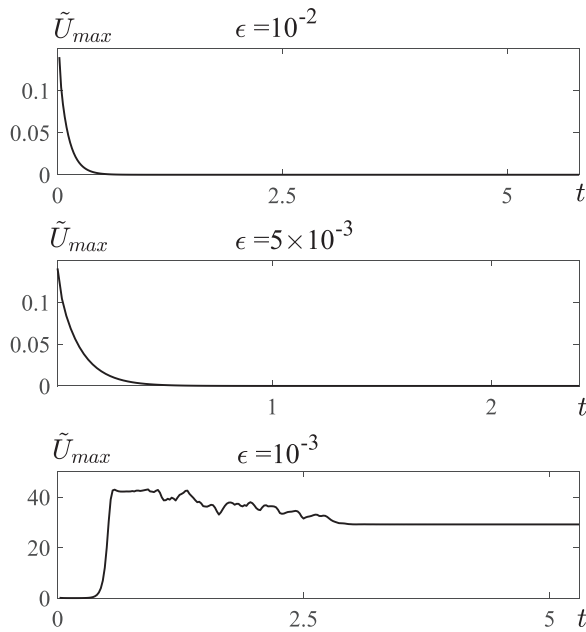


FIG. 9. Time evolution of the maximum velocity $\tilde{U}_{max}(t)$ for the effective Rayleigh number $Ra_T = 0.5$, $\alpha = 0.5$ and shear number $Sh = 1$, and at different values of the scale separation parameter $\epsilon = 10^{-3}, 5 \times 10^{-3}, 10^{-2}$, for the no-slip boundary conditions.

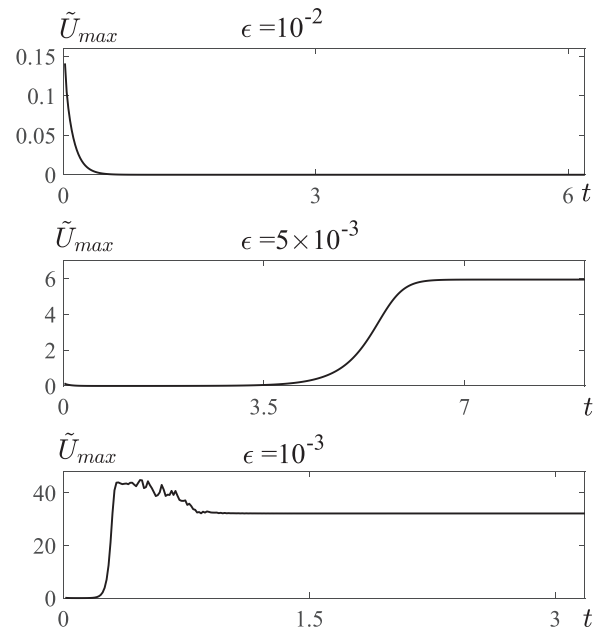


FIG. 11. Time evolution of the maximum velocity $\tilde{U}_{max}(t)$ for the effective Rayleigh number $Ra_T = 1000$, $\alpha = 0.5$ and shear number $Sh = 1$, and at different values of the scale separation parameter $\epsilon = 10^{-3}, 5 \times 10^{-3}, 10^{-2}$, for the no-slip boundary conditions.

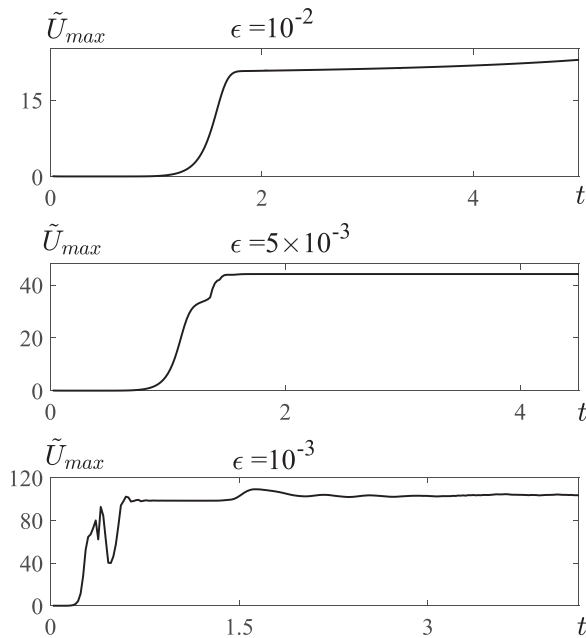


FIG. 10. Time evolution of the maximum velocity $\tilde{U}_{max}(t)$ for the effective Rayleigh number $Ra_T = 1000$, $\alpha = 0.5$ and shear number $Sh = 1$, and at different values of the scale separation parameter $\epsilon = 10^{-3}, 5 \times 10^{-3}, 10^{-2}$, for the stress-free boundary conditions.

been seen after the steady-state stage (when the function \tilde{U}_{max} is nearly constant in time) in the large-scale shear-free convection.⁵³

To observe spatial structure of the basic characteristics of the sheared large-scale convection, in Figs. 12–16 we plot the patterns of velocity vectors $\tilde{\mathbf{U}} = \tilde{U}_y \mathbf{e}_y + \tilde{U}_z \mathbf{e}_z$ with $\tilde{U}_x \rightarrow 0$ (panel a); the patterns of the potential temperature deviations $\tilde{\Theta} Ra_T$ from the equilibrium potential temperature in the basic reference state (panel b) and the patterns of the vertical gradient of the mean potential temperature $(\nabla_z \tilde{\Theta} - 1) Ra_T$ (panel c) at several time instants: before the system reaches steady state (see Figs. 12 and 13) and after the system reaches steady state (see Fig. 14–16). Here, \mathbf{e}_x , \mathbf{e}_y , and \mathbf{e}_z are the unit vectors directed along the x , y , and z axes.

We remind that the potential temperature is measured in the units of $L_z N^2 Pr_T / \beta = Ra_T \nu_T^2 / (\beta L_z^3)$. This is the reason why we show in Figs. 12–16 (see panels b) the pattern of the normalized deviations of the potential temperature $\tilde{\Theta} Ra_T$ from the equilibrium potential temperature in the basic reference state. Note also that the total gradient of the potential temperature is the sum of the equilibrium constant gradient of the potential temperature $\nabla_z \bar{T}_{eq}$ (negative for a convection) and the gradient of the potential temperature $\nabla_z \tilde{\Theta}$. Therefore, we show in Figs. 12–16 (see panels c) the pattern of the normalized total vertical gradient of the mean potential temperature, $(\nabla_z \tilde{\Theta} - 1) Ra_T$, which characterizes the large-scale convection.

At the linear stage of the system evolution, the patterns for the stress-free and no-slip boundary conditions are the same (see Fig. 17 shown in the yz plane, where in the panel (a) we plot the patterns of velocity vectors $\tilde{\mathbf{U}} = \tilde{U}_y \mathbf{e}_y + \tilde{U}_z \mathbf{e}_z$ with $\tilde{U}_x \rightarrow 0$). During the evolution, there is a transition from the large-scale circulations at the yz plane seen in the linear stage of the instability (see Fig. 17) to the large-scale circulations at the xz plane observed during the nonlinear stage

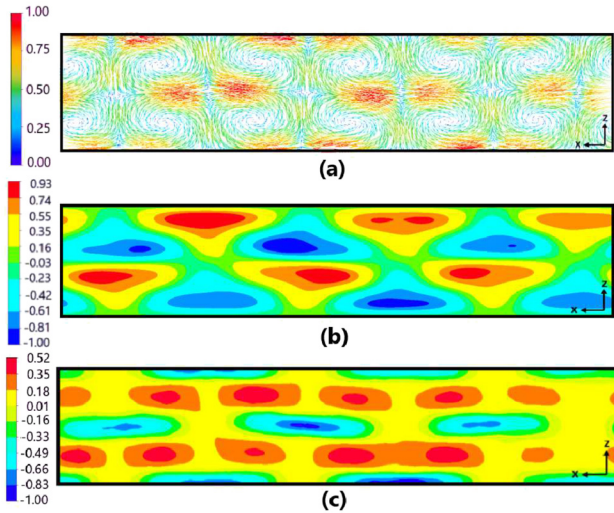


FIG. 12. The patterns of velocity vectors $\tilde{U} = \tilde{U}_x e_x + \tilde{U}_z e_z$ with $\tilde{U}_y \rightarrow 0$ [Fig. 12(a)]; the patterns of the potential temperature deviations ΘRa_T from the equilibrium potential temperature in the basic reference state [Fig. 12(b)]; the patterns of the vertical gradient of the mean potential temperature $(\nabla_z \Theta - 1) Ra_T$ [Fig. 12(c)] at time instant $t = 0.34$ of the turbulent viscosity time L_z^2/ν_T , effective Rayleigh number $Ra_T = 0.5$, $\epsilon = 10^{-3}$, $\alpha = 0.5$ and shear number $Sh = 1$ for the stress-free vertical boundary conditions. All quantities are normalized by their maximum values.

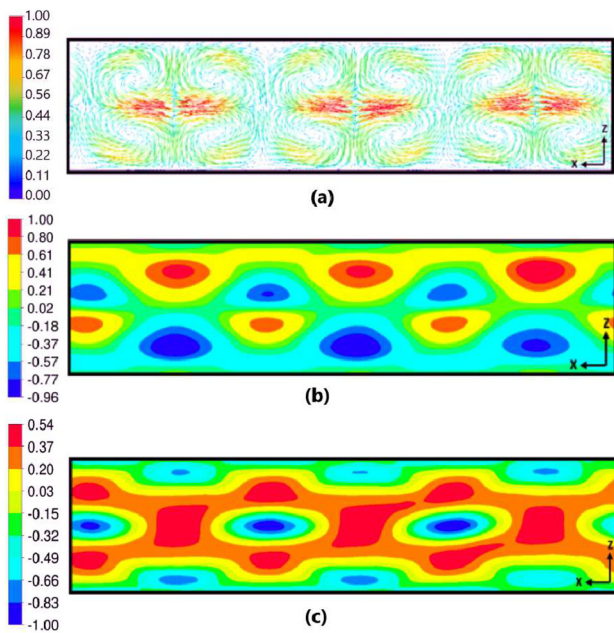


FIG. 13. The patterns of velocity vectors $\tilde{U} = \tilde{U}_x e_x + \tilde{U}_z e_z$ with $\tilde{U}_y \rightarrow 0$ [Fig. 13(a)]; the patterns of the potential temperature deviations ΘRa_T from the equilibrium potential temperature in the basic reference state [Fig. 13(b)]; the patterns of the vertical gradient of the mean potential temperature $(\nabla_z \Theta - 1) Ra_T$ [Fig. 13(c)] at time instant $t = 0.7$ of the turbulent viscosity time L_z^2/ν_T , effective Rayleigh number $Ra_T = 0.5$, $\epsilon = 10^{-3}$, $\alpha = 0.5$ and shear number $Sh = 1$ for the no-slip vertical boundary conditions. All quantities are normalized by their maximum values.

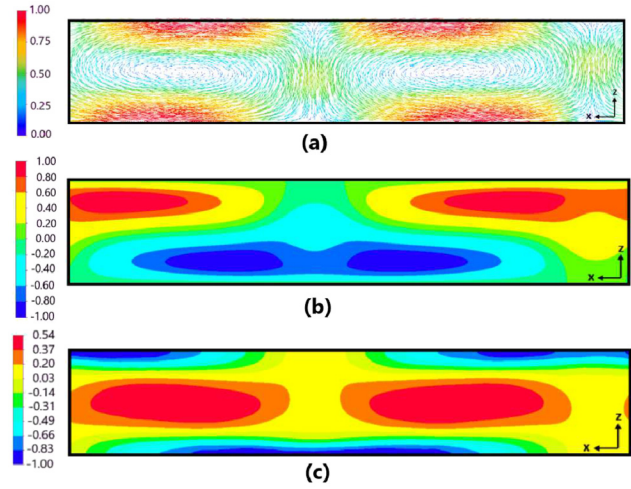


FIG. 14. The patterns of velocity vectors $\tilde{U} = \tilde{U}_x e_x + \tilde{U}_z e_z$ with $\tilde{U}_y \rightarrow 0$ [Fig. 14(a)]; the patterns of the potential temperature deviations ΘRa_T from the equilibrium potential temperature in the basic reference state [Fig. 14(b)]; the patterns of the vertical gradient of the mean potential temperature $(\nabla_z \Theta - 1) Ra_T$ [Fig. 14(c)] at time instant $t = 1$ of the turbulent viscosity time L_z^2/ν_T , effective Rayleigh number $Ra_T = 0.5$, $\epsilon = 10^{-3}$, $\alpha = 0.5$ and shear number $Sh = 1$ for the stress-free vertical boundary conditions. All quantities are normalized by their maximum values.

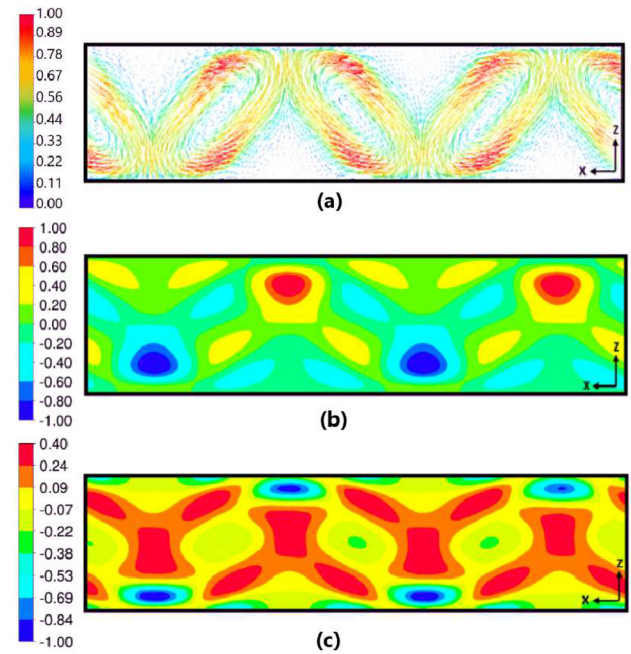


FIG. 15. The patterns of velocity vectors $\tilde{U} = \tilde{U}_x e_x + \tilde{U}_z e_z$ with $\tilde{U}_y \rightarrow 0$ [Fig. 15(a)]; the patterns of the potential temperature deviations ΘRa_T from the equilibrium potential temperature in the basic reference state [Fig. 15(b)]; the patterns of the vertical gradient of the mean potential temperature $(\nabla_z \Theta - 1) Ra_T$ [Fig. 15(c)] at time instant $t = 4$ of the turbulent viscosity time L_z^2/ν_T , effective Rayleigh number $Ra_T = 0.5$, $\epsilon = 10^{-3}$, $\alpha = 0.5$ and shear number $Sh = 1$ for the no-slip vertical boundary conditions. All quantities are normalized by their maximum values.

10 July 2024 14:13:34

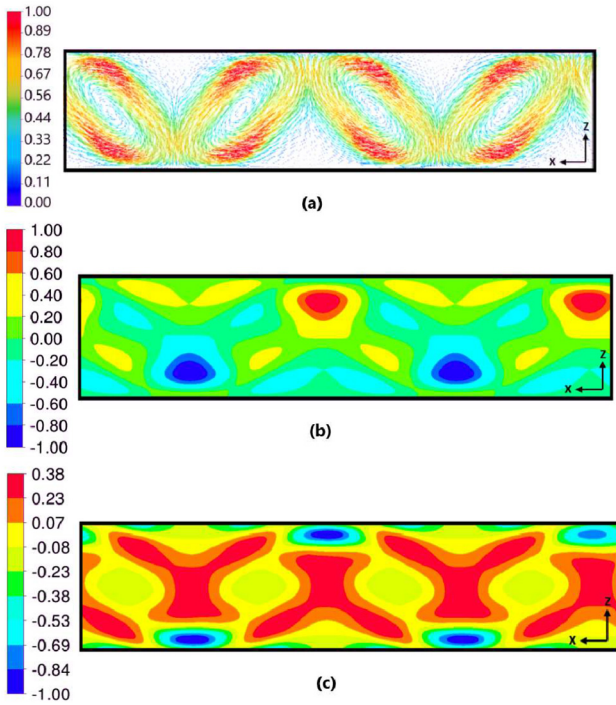


FIG. 16. The patterns of velocity vectors $\vec{U} = \tilde{U}_x \mathbf{e}_x + \tilde{U}_z \mathbf{e}_z$ with $\tilde{U}_y \rightarrow 0$ [Fig. 16(a)]; the patterns of the potential temperature deviations ΘRa_T from the equilibrium potential temperature in the basic reference state [Fig. 16(b)]; the patterns of the vertical gradient of the mean potential temperature $(\nabla_z \Theta - 1) \text{Ra}_T$ [Fig. 16(c)] at time instant $t = 5.32$ of the turbulent viscosity time L_z^2/ν_T , effective Rayleigh number $\text{Ra}_T = 1000$, $\epsilon = 10^{-3}$, $\alpha = 0.5$ and shear number $\text{Sh} = 1$ for the no-slip vertical boundary conditions. All quantities are normalized by their maximum values.

of the instability (see Figs. 12 and 13). In addition, there is a transition from the two-layer vertical structure of the mean velocity field with two convective rolls in the z direction and six rolls in the x direction (as can be seen in Fig. 12 for the stress-free boundary conditions) to the one-layer vertical structure with one roll in the z direction and two rolls in the x direction (see Fig. 14).

On the other hand, comparing Figs. 13 and 15 (which corresponds to the no-slip boundary conditions), we observe that during nonlinear stage of the instability there is a transition from the large-scale circulations with the two-layer vertical structure with two convective rolls in the z direction and six rolls in the x direction (see Fig. 13) to the one-layer structure with four inclined rolls (see Fig. 15). The formation of the inclined rolls for the no-slip boundary conditions are already observed starting with $t = 0.9$ of the turbulent viscosity time L_z^2/ν_T at the effective Rayleigh number $\text{Ra}_T = 0.5$. The inclined rolls for the no-slip boundary conditions are also observed at the effective Rayleigh number $\text{Ra}_T = 10^3$ (see Fig. 16).

As has been observed in the shear-free convection,⁵³ the large-scale convective structures are also formed in a sheared convection even at low values of the effective Rayleigh numbers $\text{Ra}_T = 0.5$ due to the additional terms proportional to ϵ in Eq. (5) for the evolution of the potential temperature (which are caused by the modification of the turbulent heat flux by non-uniform fluid flows). Moreover, in Figs.

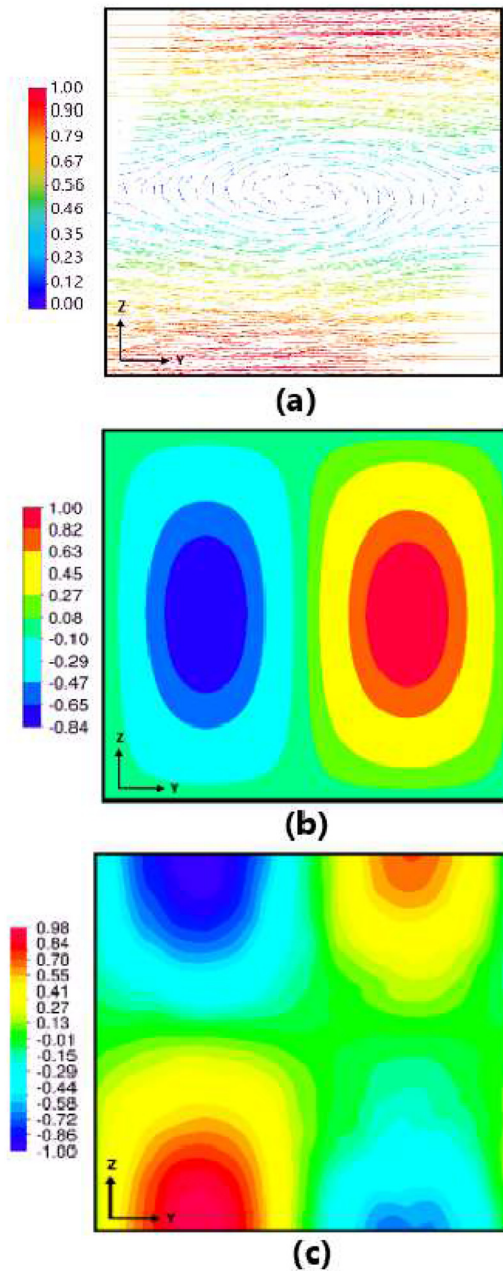


FIG. 17. The patterns of velocity vectors $\vec{U} = \tilde{U}_y \mathbf{e}_y + \tilde{U}_z \mathbf{e}_z$ with $\tilde{U}_x \rightarrow 0$ [Fig. 17(a)]; the patterns of the potential temperature deviations ΘRa_T from the equilibrium potential temperature in the basic reference state [Fig. 17(b)]; the patterns of the vertical gradient of the mean potential temperature $(\nabla_z \Theta - 1) \text{Ra}_T$ [Fig. 17(c)] at time instant $t = 0.04$ of the turbulent viscosity time L_z^2/ν_T , effective Rayleigh number $\text{Ra}_T = 0.5$, $\epsilon = 10^{-3}$, $\alpha = 0.5$ and shear number $\text{Sh} = 1$ for the stress-free vertical boundary conditions. All quantities are normalized by their maximum values.

12–16 (panel c), one can see the regions with the positive gradient of the potential temperature $(\nabla_z \Theta - 1) \text{Ra}_T$, which are typical for stably stratified turbulence. Such effects have been previously observed in experiments,^{16,57} direct numerical simulations^{44,46,47,58} of turbulent

convection and shear-free mean-field numerical simulations.⁵³ The formation of the regions with the positive gradient of the potential temperature inside the large-scale circulation can be understood as follows. The total vertical heat flux F_z^{tot} includes three contributions⁵³:

- the mean vertical heat flux $\overline{U}_z \overline{\Theta}$ of the large-scale circulation,
- the vertical turbulent heat flux $F_z^* = -\kappa_T \nabla_z \overline{\Theta}$, and
- the new turbulent heat flux $F_z^{\text{new}} = -\tau_0 F_z^* \text{div } \overline{U}_\perp$.

Therefore, the vertical gradient $\nabla_z \overline{\Theta}$ of the mean potential temperature is given by

$$\nabla_z \overline{\Theta} = \frac{\overline{U}_z \overline{\Theta} - F_z^{\text{tot}}}{\kappa_T (1 - \tau_0 \text{div } \overline{U}_\perp)}. \quad (21)$$

Inside the large-scale circulation where $\overline{U}_z \overline{\Theta} > F_z^{\text{tot}}$, the vertical gradient $\nabla_z \overline{\Theta}$ is positive. On the other hand, when $\overline{U}_z \overline{\Theta} < F_z^{\text{tot}}$, the vertical gradient $\nabla_z \overline{\Theta}$ is negative. Here, we take into account that $\tau_0 |\text{div } \overline{U}_\perp| < 1$.

In the present study, we also observe the formation the large-scale rolls even below the threshold of the laminar convection (see Figs. 12–15 for effective Rayleigh number $\text{Ra}_T = 0.5$, which can be compared with Fig. 16 for $\text{Ra}_T = 1000$). This is because turbulence with non-uniform large-scale flows contributes to the turbulent heat flux. The reasons for this effect are related to the production of additional essentially anisotropic velocity fluctuations generated by tangling of the mean-velocity gradients by small-scale turbulent motions due to the influence of the inertial forces during the lifetime of turbulent eddies. These anisotropic velocity fluctuations contribute to the turbulent heat flux. In particular, anisotropic velocity fluctuations $\mathbf{u}^{\text{anisot}}$ are produced by the large-scale shear $\nabla_j \overline{U}_i$ in the presence of isotropic velocity fluctuations \mathbf{u}^{isot} , i.e., $\partial \mathbf{u}^{\text{anisot}} / \partial t \propto -(\mathbf{u}^{\text{isot}} \cdot \nabla) \overline{U}_i$. This mechanism is called “tangling”. Similar mechanism exists in fluid dynamics, when temperature fluctuations θ are produced by “tangling” of the gradient of the mean temperature $\nabla_j \overline{T}$ by velocity fluctuations \mathbf{u} , i.e., $\partial \theta / \partial t \propto -(\mathbf{u} \cdot \nabla) \overline{T}$. Moreover, the tangling mechanism also exists in magnetohydrodynamics, when magnetic fluctuations \mathbf{b} are produced by “tangling” of the mean magnetic field $\overline{\mathbf{B}}$ by velocity fluctuations, i.e., $\partial \mathbf{b} / \partial t \propto (\overline{\mathbf{B}} \cdot \nabla) \mathbf{u}$. So, the “tangling” is an universal mechanism of production of anisotropic fluctuations.

The modification of the turbulent heat flux by anisotropic velocity fluctuations causes an excitation of large-scale convective-shear instability, which results in the formation of large-scale semi-organized structures in the form of rolls and generation of convective-shear waves propagating perpendicular to the convective rolls. The lifetimes and spatial scales of these structures are much larger compared to the largest turbulent time scales. As the result, the evolutionary equation (5) for the potential temperature $\overline{\Theta}$ contains the new terms proportional to the spatial derivatives of the mean velocity field \overline{U} (see the terms proportional to the parameter ϵ).

The developed mean-field theory, which yields a convective-shear instability, is capable of explaining the properties of semi-organized structures observed in the atmospheric convective boundary layer. In particular, in the presence of the mean wind, the semi-organized structures are observed in the form of rolls (cloud streets). The observed rolls usually align along the mean horizontal wind of the convective layer, with lengths varying from 20 to 200 km, widths changing from 2 to 10 km, and convective depths varying from 2 to 3 km.³⁰ The typical value of the aspect ratio of the observed rolls is

$L_z^{\text{cs}} / L_h^{\text{cs}} \approx 0.14$ –1, where L_z^{cs} and L_h^{cs} are the vertical and horizontal scales of the cloud streets in the plane perpendicular to the mean wind. The ratio of the minimal size L^{cs} of the observed structures to the integral scale of turbulent motions is $L^{\text{cs}} / \ell_0 = 10$ –100. The characteristic lifetime of rolls varies from 1 to 10 h. The suggested theory predicts the following parameters of the convective rolls: the aspect ratio $L_z^{\text{cs}} / L_h^{\text{cs}}$ ranges from very small values to 1, and L^{cs} / ℓ_0 varies from 10 to 100. The characteristic time of formation of the rolls $\sim \tau_0 / \gamma_{\text{inst}}$ varies from 1 to 3 h. It is of the order of several turbulent viscosity time.

V. CONCLUSIONS

Mean-field simulations based on a developed mean-field theory^{50,51} of a non-rotating sheared turbulent convection are performed. This mean-field theory describes an effect of modification of the turbulent heat flux by the non-uniform large-scale motions caused by production of essentially anisotropic velocity fluctuations generated by tangling of the mean-velocity gradients by small-scale turbulent motions. The effect causes an excitation of large-scale convective-shear instability and the formation of large-scale convective rolls. During the nonlinear stage of the convective-shear instability, there is a transition from a two-layer vertical structure with two rolls in the vertical direction before the system reaches steady state to a one-layer vertical structure with one roll after the system reaches steady state. This effect is observed for all effective Rayleigh numbers.

The performed mean-field simulations show that the modification of the turbulent heat flux by the non-uniform large-scale motions results in a strong decrease in the critical effective Rayleigh number required for the formation of the large-scale rolls. These mean-field simulations have demonstrated that the spatial distribution of the mean potential temperature has regions with a positive vertical gradient of the potential temperature inside the convective roll due to the mean heat flux of the convective rolls. This study might be useful for understanding the origin of large-scale rolls observed in atmospheric convective boundary layers, as well as in numerical simulations and laboratory experiments.

ACKNOWLEDGMENTS

I.R. would like to acknowledge the Isaac Newton Institute for Mathematical Sciences, Cambridge, for support and hospitality during the programme “Anti-diffusive dynamics: from sub-cellular to astrophysical scales,” where the final version of the paper was completed. The work of N.K. was partially supported by the Russian Science Foundation (Grant No. 21-72-20067). The authors benefited from stimulating discussions of various aspects of turbulent convection with A. Brandenburg and P. J. Käpylä.

AUTHOR DECLARATIONS

Conflict of Interest

The authors have no conflicts to disclose.

Author Contributions

A. Asulin: Data curation (equal); Formal analysis (equal); Investigation (equal); Validation (equal). **E. Tkachenko:** Data curation (equal); Investigation (equal). **N. Kleeorin:** Conceptualization (equal); Formal analysis (equal); Investigation (equal); Methodology (equal);

Supervision (equal); Validation (equal); Writing – original draft (equal). **A. Levy:** Conceptualization (equal); Formal analysis (equal); Investigation (equal); Methodology (equal); Supervision (equal); Validation (equal); Writing – original draft (equal); Writing – review & editing (equal). **I. Rogachevskii:** Conceptualization (equal); Formal analysis (equal); Investigation (equal); Methodology (equal); Supervision (equal); Validation (equal); Writing – original draft (equal); Writing – review & editing (equal).

DATA AVAILABILITY

The data that support the findings of this study are available from the corresponding author upon reasonable request.

REFERENCES

- ¹S. Chandrasekhar, *Hydrodynamic and Hydromagnetic Stability* (Oxford University Press, Oxford, 1961).
- ²J. S. Turner, *Buoyancy Effects in Fluids* (Cambridge University Press, Cambridge, 1973).
- ³S. S. Zilitinkevich, *Turbulent Penetrative Convection* (Avebury Technical, Aldershot, 1991).
- ⁴E. Bodenschatz, W. Pesch, and G. Ahlers, “Recent developments in Rayleigh-Bénard convection,” *Annu. Rev. Fluid Mech.* **32**, 709 (2000).
- ⁵G. Ahlers, S. Grossmann, and D. Lohse, “Heat transfer and large scale dynamics in turbulent Rayleigh-Bénard convection,” *Rev. Mod. Phys.* **81**, 503 (2009).
- ⁶D. Lohse and K.-Q. Xia, “Small-scale properties of turbulent Rayleigh-Bénard convection,” *Annu. Rev. Fluid Mech.* **42**, 335 (2010).
- ⁷Q. Zhou and K.-Q. Xia, “The mixing evolution and geometric properties of a passive scalar field in turbulent Rayleigh-Bénard convection,” *New J. Phys.* **12**, 083029 (2010).
- ⁸A. S. Monin and A. M. Yaglom, *Statistical Fluid Mechanics* (Dover, New York, 2013).
- ⁹M. Lesieur, *Turbulence in Fluids* (Springer, Dordrecht, 2008).
- ¹⁰P. A. Davidson, *Turbulence in Rotating, Stratified and Electrically Conducting Fluids* (Cambridge University Press, Cambridge, 2013).
- ¹¹E. S. C. Ching, *Statistics and Scaling in Turbulent Rayleigh-Bénard Convection* (Springer, Singapore, 2014).
- ¹²I. Rogachevskii, *Introduction to Turbulent Transport of Particles, Temperature and Magnetic Fields* (Cambridge University Press, Cambridge, 2021).
- ¹³R. Krishnamurti and L. N. Howard, “Large-scale flow generation in turbulent convection,” *Proc. Natl. Acad. Sci. U. S. A.* **78**, 1981 (1981).
- ¹⁴M. Sano, X. Z. Wu, and A. Libchaber, “Turbulence in helium-gas free convection,” *Phys. Rev. A* **40**, 6421 (1989).
- ¹⁵S. Ciliberto, S. Cioni, and C. Laroche, “Large-scale flow properties of turbulent thermal convection,” *Phys. Rev. E* **54**, R5901 (1996).
- ¹⁶J. J. Niemela, L. Skrbek, K. R. Sreenivasan, and R. J. Donnelly, “The wind in confined thermal convection,” *J. Fluid Mech.* **449**, 169 (2001).
- ¹⁷J. J. Niemela and K. R. Sreenivasan, “Rayleigh-number evolution of large-scale coherent motion in turbulent convection,” *Europhys. Lett.* **62**, 829 (2003).
- ¹⁸U. Burr, W. Kinzelbach, and A. Tsinober, “Is the turbulent wind in convective flows driven by fluctuations?,” *Phys. Fluids* **15**, 2313 (2003).
- ¹⁹H. D. Xi, S. Lam, and X. Q. Xia, “From laminar plumes to organized flows: The onset of large-scale circulation in turbulent thermal convection,” *J. Fluid Mech.* **503**, 47 (2004).
- ²⁰D. Funfschilling and G. Ahlers, “Plume motion and large-scale circulation in a cylindrical Rayleigh-Bénard cell,” *Phys. Rev. Lett.* **92**, 194502 (2004).
- ²¹E. Brown, A. Nikolaenko, and G. Ahlers, “Orientation changes of the large-scale circulation in turbulent Rayleigh-Bénard convection,” *Phys. Rev. Lett.* **95**, 084503 (2005).
- ²²A. Liberzon, B. Lüthi, M. Guala, W. Kinzelbach, and A. Tsinober, “Experimental study of the structure of flow regions with negative turbulent kinetic energy production in confined three-dimensional shear flows with and without buoyancy,” *Phys. Fluids* **17**, 095110 (2005).
- ²³A. Eidelman, T. Elperin, N. Kleeorin, A. Markovich, and I. Rogachevskii, “Hysteresis phenomenon in turbulent convection,” *Exp. Fluids* **40**, 723 (2006).
- ²⁴D. Funfschilling, E. Brown, and G. Ahlers, “Torsional oscillations of the large-scale circulation in turbulent Rayleigh-Bénard convection,” *J. Fluid Mech.* **607**, 119 (2008).
- ²⁵M. Bukai, A. Eidelman, T. Elperin, N. Kleeorin, I. Rogachevskii, and I. Sapir-Katiraie, “Effect of large-scale coherent structures on turbulent convection,” *Phys. Rev. E* **79**, 066302 (2009).
- ²⁶M. Bukai, A. Eidelman, T. Elperin, N. Kleeorin, I. Rogachevskii, and I. Sapir-Katiraie, “Transition phenomena in unstably stratified turbulent flows,” *Phys. Rev. E* **83**, 036302 (2011).
- ²⁷J. C. Kaimal and J. J. Fennigan, *Atmospheric Boundary Layer Flows* (Oxford University Press, New York, 1994).
- ²⁸D. Etling, “Some aspects on helicity in atmospheric flows,” *Contrib. Atmos. Phys.* **58**, 88 (1985).
- ²⁹D. Etling and R. A. Brown, “Roll vortices in the planetary boundary layer: A review,” *Boundary-Layer Meteorol.* **65**, 215 (1993).
- ³⁰B. W. Atkinson and J. Wu Zhang, “Mesoscale shallow convection in the atmosphere,” *Rev. Geophys.* **34**, 403, <https://doi.org/10.1029/96RG02623> (1996).
- ³¹B. Brümmner, “Roll and cell convection in winter-time arctic cold-air outbreaks,” *J. Atmos. Sci.* **56**, 2613 (1999).
- ³²G. S. Young, D. A. R. Kristovich, M. R. Hjelmfelt, and R. C. Foster, “Rolls, streets, waves and more,” *Bull. Am. Meteorol. Soc.* **83**, 997 (2002).
- ³³J. C. Wyngaard, *Turbulence in the Atmosphere* (Cambridge University Press, 2010).
- ³⁴F. Tampieri, *Turbulence and Dispersion in the Planetary Boundary Layer* (Springer, 2017).
- ³⁵B. Jayaraman and J. G. Brasseur, “Transition in atmospheric boundary layer turbulence structure from neutral to convective, and large-scale rolls,” *J. Fluid Mech.* **913**, A42 (2021).
- ³⁶S. Zilitinkevich, E. Kadantsev, I. Repina, E. Mortikov, and A. Glazunov, “Order out of chaos: Shifting paradigm of convective turbulence,” *J. Atmos. Sci.* **78**, 3925 (2021).
- ³⁷I. Rogachevskii, N. Kleeorin, and S. Zilitinkevich, “Energy-and flux-budget theory for surface layers in atmospheric convective turbulence,” *Phys. Fluids* **34**, 116602 (2022).
- ³⁸I. Rogachevskii and N. Kleeorin, “Semi-organized structures and turbulence in the atmospheric convection,” *Phys. Fluids* **36**, 026610 (2024).
- ³⁹T. Hartlep, A. Tilgner, and F. H. Busse, “Large-scale structures in Rayleigh-Bénard convection at high Rayleigh numbers,” *Phys. Rev. Lett.* **91**, 064501 (2003).
- ⁴⁰A. Parodi, J. von Hardenberg, G. Passoni, A. Provenzale, and E. A. Spiegel, “Clustering of plumes in turbulent convection,” *Phys. Rev. Lett.* **92**, 194503 (2004).
- ⁴¹F. Rincon, “Anisotropy, inhomogeneity and inertial-range scalings in turbulent convection,” *J. Fluid Mech.* **563**, 43 (2006).
- ⁴²J. Schumacher, “Lagrangian dispersion and heat transport in convective turbulence,” *Phys. Rev. Lett.* **100**, 134502 (2008).
- ⁴³F. Chillà and J. Schumacher, “New perspectives in turbulent Rayleigh-Bénard convection,” *Eur. Phys. J. E* **35**, 58 (2012).
- ⁴⁴A. Brandenburg, “Stellar mixing length theory with entropy rain,” *Astrophys. J.* **832**, 6 (2017).
- ⁴⁵A. Hellsten and S. Zilitinkevich, “Role of convective structures and background turbulence in the dry convective boundary layer,” *Boundary-Layer Meteorol.* **149**, 323 (2013).
- ⁴⁶P. J. Käpylä, M. Rheinhardt, A. Brandenburg, R. Arlt, M. J. Käpylä, A. Lagg, N. Olsper, and J. Warnecke, “Extended subadiabatic layer in simulations of over-shooting convection,” *Astrophys. J. Lett.* **845**, L23 (2017).
- ⁴⁷P. J. Käpylä, “Overshooting in simulations of compressible convection,” *Astron. Astrophys.* **631**, A122 (2019).
- ⁴⁸J. Schumacher and K. R. Sreenivasan, “Colloquium: Unusual dynamics of convection in the Sun,” *Rev. Mod. Phys.* **92**, 041001 (2020).
- ⁴⁹A. Pandey, J. Schumacher, and K. R. Sreenivasan, “Non-Boussinesq low-Prandtl-number convection with a temperature-dependent thermal diffusivity,” *Astrophys. J.* **907**, 56 (2021).
- ⁵⁰T. Elperin, N. Kleeorin, I. Rogachevskii, and S. S. Zilitinkevich, “Formation of large-scale semi-organized structures in turbulent convection,” *Phys. Rev. E* **66**, 066305 (2002).

- ⁵¹T. Elperin, N. Kleeorin, I. Rogachevskii, and S. S. Zilitinkevich, “Tangling turbulence and semi-organized structures in convective boundary layers,” *Boundary-Layer Meteorol.* **119**, 449–472 (2006).
- ⁵²T. Elperin, I. Golubev, N. Kleeorin, and I. Rogachevskii, “Large-scale instabilities in a nonrotating turbulent convection,” *Phys. Fluids* **18**, 126601 (2006).
- ⁵³G. Orian, A. Asulin, E. Tkachenko, N. Kleeorin, A. Levy, and I. Rogachevskii, “Large-scale circulations in a shear-free convective turbulence: Mean-field simulations,” *Phys. Fluids* **34**, 105121 (2022).
- ⁵⁴E. Elmakies, O. Shildkrot, N. Kleeorin, A. Levy, and I. Rogachevskii, “Experimental study of turbulent thermal diffusion of particles in an inhomogeneous forced convective turbulence,” *Phys. Fluids* **35**, 095123 (2023).
- ⁵⁵P. J. Käpylä, A. Brandenburg, N. Kleeorin, M. J. Käpylä, and I. Rogachevskii, “Magnetic flux concentrations from turbulent stratified convection,” *Astron. Astrophys.* **588**, A150 (2016).
- ⁵⁶P. J. Käpylä, “Convective scale and subadiabatic layers in simulations of rotating compressible convection,” *Astron. Astrophys.* **683**, A221 (2024).
- ⁵⁷L. Barel, A. Eidelman, T. Elperin, G. Fleurov, N. Kleeorin, A. Levy, I. Rogachevskii, and O. Shildkrot, “Detection of standing internal gravity waves in experiments with convection over a wavy heated wall,” *Phys. Fluids* **32**, 095105 (2020).
- ⁵⁸S. Toppaladoddi, S. Succi, and J. S. Wettlaufer, “Roughness as a route to the ultimate regime of thermal convection,” *Phys. Rev. Lett.* **118**, 074503 (2017).